number of high-stress-drop events that occur on their edges.

Based on our analysis of source parameters, two types of microearthquakes appear to be taking place around the aseismic zones. The most common type is a background seismicity of uniformly distributed low-stress-drop (<1 bar) events. Less common are higher-stress-drop (1 to 10 bars) events, which tend to cluster around the asperities. Perhaps these less common events represent the transition between weak and strong parts of the fault zone.

We propose that this character of the microearthquakes is related to the locking up of the San Andreas fault in this region. Our proposal comes from the observation that as events from the creeping fault section northwest of the network are progressively eliminated, the departure from $b = -1$ is progressively larger (Fig. 4). In our model, slip at any point on the fault is a combination of earthquake ruptures and creep, the relative proportion of which might account for the relative numbers of small and large microearthquakes. Perhaps at locations where the fault is strong for longer times and distances, such as at the Parkfield asperities, small displacements are mostly expressed as creep events over large planes. At locations where the fault is easily broken at shorter distance and time scales, small microearthquakes can take place as well as creep, as seems to be happening to the north of Parkfield.

The DDSN catalogue of microseismicity provides a baseline that can be used in monitoring the earthquake process at Parkfield. The evolution of the aseismic zones and high-stress-drop events may provide clues to the mechanics of moderate earthquakes. Likewise, changes in the proportions of smaller microearthquakes, larger microearthquakes, and fault creep may indicate what time- and length-scale factors are controlling slip on this part of the San Andreas fault.

REFERENCES AND NOTES

1. The Parkfield Downhole Digital Seismic Network (DDSN) has been a joint effort between the University of California, Santa Barbara; the University of California, Berkeley; and the U.S. Geological Survey. After prototype downhole stations at Parkfield were tested in 1984 and 1985, construction of the DDSN was begun in 1986 and completed in 1987. Except for the Joaquin South (JS) and Varian (V) sites, all the stations consist of gimbal-leveled three-component, 2-Hz Mark Products L22E seismometers cemented into roughly 75- to 275-m-deep boreholes. At JS, 4.5-Hz phones were installed at 150 m; at V, the phones were installed every few hundred meters to a depth of 1 km.
2. M. Alvarez *et al.*, *Eos* **68**, 1357 (1987).
3. P. Malin, T. McEvilly, T. Moses, *ibid.*, p. 1357 (1987) (abstr.).
4. W. H. Bakun and T. V. McEvilly, *Science* **205**, 1375 (1979).
5. W. H. Bakun and A. G. Lindh, *ibid.* **229**, 619 (1985).
6. J. P. Eaton, M. E. O'Neill, J. N. Murdock, *Bull. Seismol. Soc. Am.* **60**, 1151 (1970).
7. A. G. Lindh and D. M. Boore, *ibid.* **71**, 95 (1981).
8. M. E. O'Neill, *ibid.* **74**, 27 (1984).
9. C. M. Poley *et al.*, *Nature* **327**, 134 (1987).
10. A. J. Michael, *Eos* **69**, 1311 (1988).
11. W. H. Bakun, *ibid.* **74**, 439 (1984).
12. T. Hanks and W. Thatcher, *J. Geophys. Res.* **77**, 4393 (1972).
13. D. J. Andrews, in *Earthquake Source Mechanics*, K. Aki and P. Richards, Eds. (Monograph 37, American Geophysical Union, Washington, DC, 1986), pp. 259–267.
14. After location was determined, the moment and corner frequencies of each event were calculated from the S-wave velocity and displacement power spectra as observed at the VC station (*13*). First, the areas under the above-noise parts of the spectra were calculated by numerical integration. Then, assuming a Brune-type model of the source spectra (*12*), we used the two areas to find the equivalent zero frequency intercept and the characteristic roll-off (corner frequency). With the difference in arrival times between the P- and S-waves at VC and an assumed S-wave velocity of 3.5 km/s, the moment of each event was obtained. The moments of 32 larger events were correlated against their reported California Seismic Network (CALNET) magnitudes, with the result that $M_{\mathrm{USGS}} = 0.83 \operatorname{Log} M_0 - 14.61$ (± 0.2), where M_0 is our calculated moment and M_{USGS} the U.S. Geological Survey established local magnitude scale (*11*); all magnitudes are reported as M_{USGS}.
15. For clarity and brevity the locations of the high-stress-drop events have not been shown explicitly in Figs. 1 and 2 nor in a separate plot. The clustering of the highest stress drops above, below, and to the side of the aseismic patches can be inferred from Fig. 3F.
16. R. S. Cockerham and J. P. Eaton, *U.S. Geol. Surv. Bull.* **1639**, 15 (1987).
17. C. Mendoza and S. H. Hartzell, *Bull Seismol. Soc. Am.* **78**, 1438 (1988).
18. R. Harris and P. Segall, *J. Geophys. Res.* **92**, 7945 (1987).
19. H.-P. Liu, thesis, California Institute of Technology, Pasadena (1983).

20. We thank numerous workers at the University of California, Berkeley, and the U.S. Geological Survey for the data in this report, including T. McEvilly, R. Clymer, D. Lippert, W. Bakun, A. Lindh, W. Ellsworth, A. Record, T. Burdette, B. Dollar, A. Michael, T. Moses, and R. Borcherdt. We thank R. Crosson and M. Woolf for the location software and A. Michael and G. Nishioka for their close cooperation and free scientific exchange during the progress of our work.

14 November 1988; accepted 27 March 1989

Long-Range Electronic Perturbations Caused by Defects Using Scanning Tunneling Microscopy

H. A. MIZES AND J. S. FOSTER

Real-space observations of long-range electronic perturbations caused by defects have been made with scanning tunneling microscopy. The defects are isolated adsorbed molecules on the surface of graphite. These defects perturb the charge density, giving periodic oscillations similar to Friedel oscillations. The oscillations have a wavelength $\sqrt{3}$ times that of the graphite lattice, and the symmetry of the oscillations reflects the nature of the defect.

The scanning tunneling microscope (STM), an important tool for characterizing solid surfaces with atomic resolution, has recently been used to manipulate and subsequently to observe these surfaces (*1–7*). In this report, we describe and explain peculiarities of the graphite surface that are associated with isolated adsorbed molecules (*8*). Frequently, these adsorbed molecules strongly perturb the surface electronic charge density, giving rise to periodic oscillations that emanate from the defect. These oscillations have the same physical origin as Friedel oscillations, the ripples in the charge density that surround point defects in metals. The images we present here are real-space observations of these oscillations. The oscillations are strikingly apparent in an STM topograph and modulate the graphite lattice with a $\sqrt{3} \times \sqrt{3}$ period. We describe the physical origin of this so-called superlattice in graphite and then show how from the symmetry of the superlattice one can determine the symmetry of the defect itself.

Figure 1 shows two examples of a superlattice effect associated with adsorbed molecules. Figure 1a shows the STM topograph that was obtained after adsorption had been induced by exposure of the graphite to ozone and ultraviolet radiation. In Fig. 1b, the adsorption of a molecular fragment of di(2-ethylhexyl)phthalate was induced by the application of a large voltage pulse to the tip while it was immersed in this liquid (*8*). Both molecules appear as bright spots in the STM topographs, indicating that there is an increased tunneling current when the tip is positioned over the molecule. Far from the adsorbed molecule, the graphite regains its typical hexagonal pattern (*9*). An additional feature, the superlattice, is seen frequently in the intermediate region. It appears that in this region the graphite has undergone a $\sqrt{3} \times \sqrt{3}$ reconstruction. The geometry of this reconstruction depends on the polar

H. A. Mizes, Xerox Webster Research Center, Webster, NY 14580.
J. S. Foster, IBM Research Division, Almaden Research Center, San Jose, CA 95120.

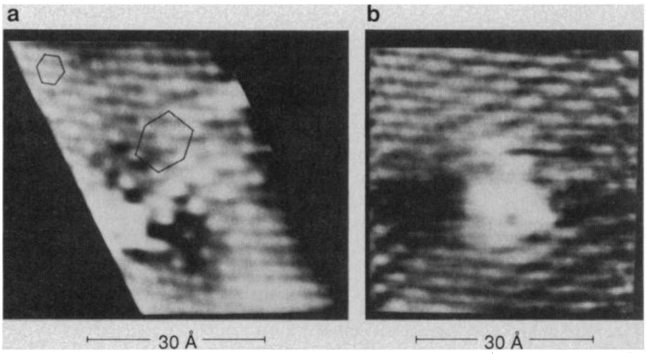

Fig. 1. (**a**) STM image of graphite after it has been exposed to ozone and ultraviolet radiation. The surface shows a low density of such defects, many of which contain a superlattice. We obtained the image by scanning the tip laterally over the surface while the feedback maintained an approximately constant tip-surface spacing with a bandwidth just less than the scanning frequency. The brighter areas correspond to regions of increased tunneling current. The shadowing effect is an electronic artifact related to the way in which the data are acquired. The six apparent graphite atoms surrounding a central atom are indicated by the hexagon in the top left of the figure, and six superlattice atoms surrounding a central atom are indicated by the hexagon near the center of the figure. (**b**) STM image of a di(2-ethylhexyl)phthalate molecule pinned to the surface of graphite by a 3.7-V pulse to the tunneling tip.

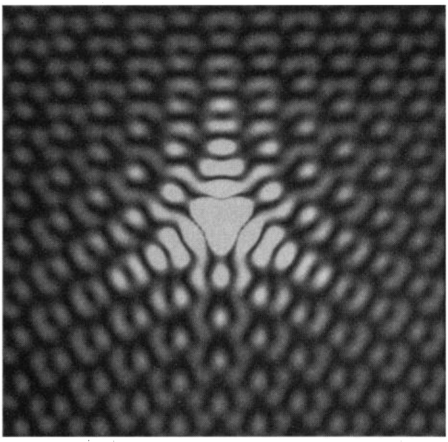

Fig. 2. Computer simulation of an STM image due to a single point defect generated as described in the text. The gray level intensity corresponds to the tunneling current for a tip scanning at a constant height. The scales in this figure and in Fig. 3 differ from that in Fig. 1 to emphasize the extent of the superlattice.

angle about the defect. We believe that the superlattice is neither the result of a physical movement of the atoms, nor an artifact of the tip, but is instead due to a change in the electron density at the Fermi energy. The superlattice is associated with various other defects, including grain boundaries and holes in the surface, and has been observed in other laboratories (*10–12*).

The physical reason for the appearance of the superlattice can be illustrated by a linear chain of atoms, with one valence electron per atom. We use a tight-binding basis to express the wave function. When the atoms are coupled, a half-filled band will form. An STM tip scanning over this chain monitors the Fermi-level charge density at the position of the tip (*13*). There are only two wave functions at the Fermi energy. Each has a wave vector of $k = \pm \pi/2d$, or a wavelength of $4d$, where d is the interatomic distance. Two independent linear combinations of these wave functions can be taken, one symmetric and one antisymmetric, about an arbitrary origin. Because the wave functions have a wavelength of $4d$, they will have nodes on every other atom. To be more specific, we can choose the origin at the position of an even atom. The contribution to the symmetric wave function occurs from only the even atoms, and the contribution to the antisymmetric wave function occurs from only the odd atoms. The charge density at the Fermi level, given by the sum of the squares of these two wave functions, will be equal over each atom (as the charge density must, because it must have the periodicity of the lattice).

Now let us suppose that this linear chain is perturbed locally, by, for example, a substitutional impurity or a bond made between an adsorbed atom and a chain atom. This localized perturbation can only cause a phase shift in the one-dimensional wave functions (*14*). For a delta-function perturbation at the origin (which in tight-binding theory is realized by perturbing just a single matrix element), the antisymmetric solution is not perturbed, because the magnitude of the wave function is zero at the origin, and there is no coupling to the perturbation. On the other hand, the symmetric wave function is perturbed. For a general perturbation, the phase shifts to the symmetric and antisymmetric wave functions will be different. If only the symmetric wave function experiences a phase shift, the wave function will be distributed now over both the even and odd atoms, whereas the antisymmetric wave function will still be concentrated on only the odd atoms. The perturbed charge density then will differ between odd and even atoms. This will appear as a superlattice superimposed on the atoms. For this one-dimensional case, the superlattice is twice the wavelength of the lattice, because the band is half-filled, and thus the Fermi wave vector is half the width of the Brillouin zone.

We now extend our one-dimensional argument to the two-dimensional graphite monolayer. This monolayer is arranged in a honeycomb lattice, and its corresponding Brillouin zone is a regular hexagon. For the monolayer, the Fermi surface collapses to points at the corners of the Brillouin zone (*15*). The layers in the full crystal are staggered, so that the monolayer has two inequivalent atoms—an A atom that is above an atom in the layer below and a B atom that is above a hollow in the layer below. The effect of the lower layers is to shift wave functions concentrated on the A atoms away from the Fermi energy, and therefore these atoms are not seen with the STM (*9, 16*). The two wave functions remaining at the Fermi energy are concentrated on the B atoms and can be expressed as a symmetric and antisymmetric linear combination of the wave vectors oriented toward the corners of the hexagonal Brillouin zone.

We choose the origin of the graphite lattice to be a B atom. Both the symmetric and antisymmetric solutions at the Fermi energy are concentrated on the B atoms. Therefore, if a single bond is made to the A atom, we do not expect to see any long-range perturbations in the STM image.

The magnitude of the graphite Fermi wave vector is $k_F = 4\pi/3\sqrt{3}d$, where d is the nearest neighbor separation. This gives rise to Bloch waves, oriented toward the corners of a hexagon, with a wavelength $3\sqrt{3}d/2$, and thus a wave function that repeats every sixth atom. Because of translational symmetry, the sum of the squares of the symmetric and antisymmetric wave functions must give rise to a charge density that is equal on every B atom.

The effect of a localized perturbation in one dimension is to shift the phase of the symmetric solution. In two dimensions the effect is to add a standing scattered wave to the symmetric solution. The antisymmetric solution remains unperturbed, because it has a zero amplitude at the origin. The sum of the squares of these two wave functions no longer has the amplitude distribution over the atoms so as to make all the B atoms equivalent. One therefore sees a lattice with only every third B atom similar, as in the images of Fig. 1. Because the perturbation in the symmetric wave function decays with distance from the scattering center, so should the superlattice. In addition, because a scattered wave decays as a power rather than exponentially, the long-range nature of the superlattice is explained. We have verified a power law decay by determining the strength of the superlattice as a function of the distance from the scattering center.

Multiple atomic tips appear frequently when graphite and other materials are being imaged; these multiple tips have been used to successfully explain the loss of threefold symmetry (*17*) and the moiré patterns observed on the graphite surface (*11*). The superlattice is not an artifact due to multiple tips but is a property of the surface electronic structure. Multiple tips can alter the phase and add Fourier components of the same magnitude but can never introduce the smaller magnitude Fourier components of the superlattice.

We have quantitatively solved for the wave functions at the Fermi energy for a bond to a single B atom, using a tight-binding model for the carbon atom orbitals and nearest neighbor interactions (*18*). We solve exactly for the non–self-consistent perturbed coefficients, using the Green function for the honeycomb lattice (*19*) and the method described by Economou (*20*). We simulate a constant-height STM image by summing the carbon p_z orbitals, using Harrison's carbon term value to calculate the decay exponent (*21*) (Fig. 2). The geometry of the superlattice varies as a function of polar angle around the defect and reflects the threefold symmetry of the graphite monolayer about the defect. In some directions the defect's effect is to increase the apparent height of every third atom, whereas in other directions it causes a superperiodic distortion of the atoms. This modulation is due to the modified electronic structure caused by the defect and is not due to any reconstruction of the atomic positions.

The experimental images do not show the threefold symmetry, evident in the simulation, that is required for a single defect. We have not yet determined the conditions that cause a single atom to adsorb to a graphite surface and thus have not observed the isotropic decay. However, we can explain the anisotropic decay by theoretically considering multiple defects. Multiple defects, which in tight-binding theory may be modeled by coupling multiple adsorbed atoms to surface atoms, can break the threefold symmetry of the lattice. The method of solution of tight-binding wave functions at the Fermi energy for multiple defects in a graphite monolayer is similar to that for the single defect. One can postulate any arrangement of adsorbates and then calculate a theoretical STM image. Four adsorbate arrangements are shown in Fig. 3. The sites to which coupling is made are indicated by the large dots atop the graphite honeycomb lattice. The strength of the coupling is equal for all bonds shown in the figure. Changing the strength of these couplings would, in general, change the nature of the image.

The nature of the superlattice varies as a function of the polar angle in a different way in each of the four images. In Fig. 3, a through c, the defects break the threefold rotational symmetry of the graphite lattice, leaving only the symmetry of reflection through a single axis. The superlattice also loses the threefold symmetry of Fig. 2 and now shows only this reflection symmetry about a single axis. In Fig. 3d, the coupling to the surface is made so that the threefold symmetry is maintained. These images give us the first hint on the identification of the adsorbates—the superlattice should reflect the symmetry of the adsorbate.

Figure 3d corresponds to the three couplings that three of the carbon atoms of the benzene molecule may make to the graphite surface. There is no superlattice associated with the image, because the scattered wave emanating from each site will differ in phase by $2\pi/3$ over any atom and far from the impurity will sum to zero. Because the phenyl group is a major constituent of organic molecules, this provides a second hint on identifying adsorbates—no superlattice should be apparent around phenyl groups. A single atom adsorbed in the center of a hexagon will cause a similar cancellation in scattering and also will not give rise to a superlattice. Our experimental images give rise to more complicated interference patterns than what arises from theory, presumably because we are observing the results of many bonds to the surface. For smaller adsorbates, we expect the experimental images to more closely resemble Figs. 2 and 3.

One last point we wish to discuss is the relation between the superlattice and Friedel oscillations. Friedel oscillations are oscillations in the electron charge density that decay away from point defects in metals. They arise from the sharp cutoff in the Fermi surface at k_F. They must be invoked to explain such diverse phenomena as nuclear magnetic resonance signal intensities (*22*), the attraction of adatoms on a surface (*23*), and the pinning of one-dimensional charge density waves (*24*). The superlattice effect occurs because of the requirement that electrons must tunnel from filled states to empty states. The current thus monitors only wave functions in a narrow energy window, that is, wave functions that have not only an upper cutoff but also a lower cutoff. These sharp cutoffs give rise to oscillations in an analogous manner.

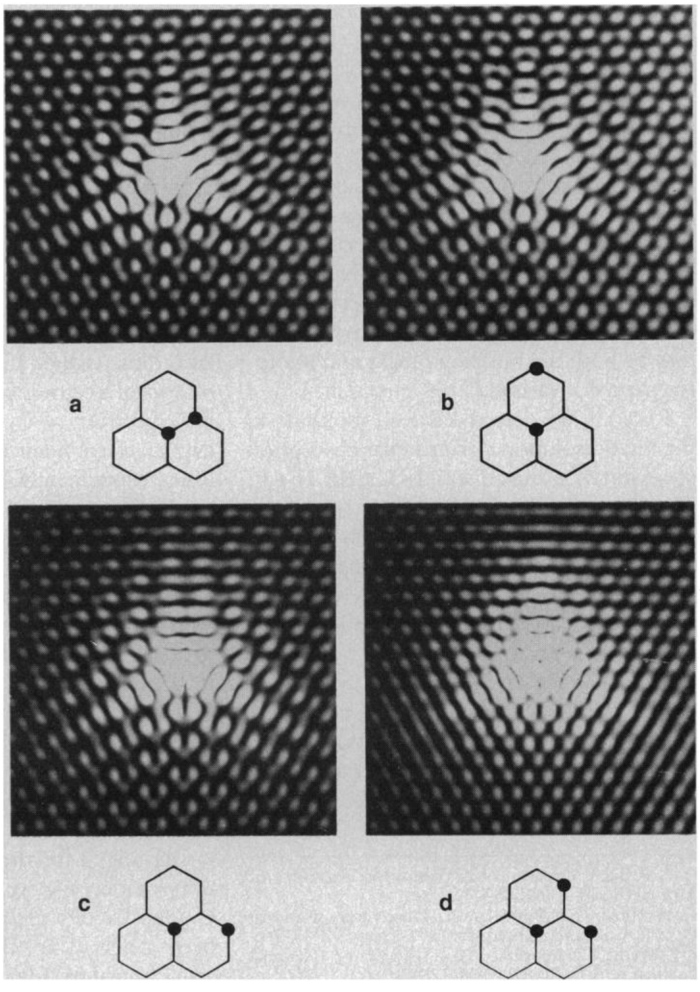

Fig. 3. Computer simulation of STM images (**a** through **d**) due to multiple point defects for four adsorbate arrangements. The bonding configuration is shown below each image. The symmetry of the superlattice reflects the symmetry of the bonding.

REFERENCES AND NOTES

1. R. S. Becker, J. A. Golovchenko, B. S. Swartzentruber, *Nature* **325**, 419 (1987).
2. R. M. Silver, E. E. Ehrichs, A. L. de Lozanne, *Appl. Phys. Lett.* **51**, 247 (1987).
3. M. A. McCord and R. F. W. Pease, *J. Vac. Sci. Technol. B* **4**, 86 (1986).
4. M. Ringger, H. R. Hedber, R. Schlogl, P. Oelhafen, H. J. Guntherudt, *Appl. Phys. Lett.* **46**, 832 (1985).
5. D. W. Abraham, H. J. Mamin, E. Ganz, J. Clarke, *IBM J. Res. Dev.* **30**, 492 (1986).
6. U. Stauter *et al.*, *Appl. Phys. Lett.* **51**, 244 (1987).
7. J. Schneir *et al.*, *J. Appl. Phys.* **63**, 717 (1988).
8. J. S. Foster, J. E. Frommer, P. C. Arnett, *Nature* **331**, 324 (1988).
9. I. P. Batra *et al.*, *Surf. Sci.* **181**, 126 (1987).
10. J. Schneir *et al.*, *Proc. Soc. Photo.-Opt. Instrum. Eng.* **897**, 16 (1988).
11. T. R. Albrecht, H. A. Mizes, J. Nogami, Sang-il Park, C. F. Quate, *Appl. Phys. Lett.* **52**, 362 (1988). In this paper the superlattice is associated with a single-tip image of the grain boundary and is not the moiré pattern associated with double tips.
12. *Phys. Today* **41** (no. 5), 129 (1988).
13. J. Tersoff and D. R. Hamann, *Phys. Rev. B* **31**, 805 (1985).
14. G. F. Koster and J. C. Slater, *Phys. Rev.* **95**, 1167 (1954); *ibid.* **96**, 1208 (1954).
15. B. T. Kelly, *Physics of Graphite* (Applied Science, London, 1981), pp. 268–284; J. Tersoff, *Phys. Rev. Lett.* **57**, 440 (1986).
16. D. Tománek *et al.*, *Phys. Rev. B* **35**, 7790 (1987).
17. H. A. Mizes, Sang-il Park, W. A. Harrison, *ibid.* **36**, 4491 (1987).
18. H. A. Mizes, thesis, Stanford University (1988).
19. T. Horiguchi, *J. Math. Phys. (N.Y.)* **13**, 1411 (1972).
20. E. N. Economou, *Green's Functions in Quantum Physics* (Springer-Verlag, New York, ed. 2, 1983).
21. W. A. Harrison, *Phys. Rev. B* **24**, 5835 (1981).
22. T. J. Rowland *Phys. Rev.* **119**, 900 (1960).
23. P. Johansson, *Solid State Commun.* **25**, 221 (1978).
24. I. Tüttö and A. Zawadowski, *Phys. Rev. B* **32**, 2449 (1985).

25. We acknowledge encouraging conversations with J. E. Frommer, W. A. Harrison, W. C. Herring, and C. F. Quate.

19 December 1988; accepted 10 March 1989

Detection of C_5 in the Circumstellar Shell of IRC+10216

PETER F. BERNATH, KENNETH H. HINKLE, JOHN J. KEADY

The C_5 molecule has been identified in the infrared spectrum of the prototypical obscured carbon star, IRC+10216. In addition to their astrophysical importance, pure carbon chain molecules such as C_5 are of interest in the chemistry of flames and propellants.

PURE CARBON MOLECULES ARE CURrently under intense experimental and theoretical scrutiny. A large number of geometrical structures are possible for C_n molecules, including chains, rings, and sheets, as well as spheroidal fullerenes (*1, 2*) such as C_{60}. These molecules are believed to play an important role in the formation of soot in flames (*1, 2*). In astrophysics, they may be both the building blocks and photofragments of carbonaceous materials.

Recently we detected the C_3 molecule in the high-resolution circumstellar absorption spectrum of a carbon star, IRC+10216 (*3*). The C_3 absorption features were very sharp (<0.014 cm^{-1} wide, full width at half-maximum) and remarkably strong (almost 50% absorbing). Inspired by these results, we searched for the "next" member of the carbon chain series, C_5.

We skipped searching for C_4 in favor of C_5 for a variety of reasons: (i) C_5 is predicted to be linear and symmetric with a closed-shell $\tilde{X}^1\Sigma_g^+$ electronic ground state similar to the C_3 molecule (*4–8*); (ii) the C_4 molecule is known to be less abundant than C_5 (*9, 10*) in high-temperature carbon vapors (although this is not necessarily the case in a circumstellar shell); and (iii) the previous infrared spectrum of C_4 (*11*) recorded near 2164 cm^{-1} in inert gas matrices was recently reassigned to C_5 (*12*).

The C_5 molecule has no dipole moment and thus cannot be monitored by pure rotational microwave spectroscopy. The optical spectrum of C_5 is not known with any degree of confidence, although some published experimental (*13*) and theoretical (*7*) suggestions are available.

The infrared vibration-rotation transitions are ideal for the detection of C_5. Of the seven vibrational modes of C_5, ν_3 (σ_u^+ symmetry) near 2164 cm^{-1} (*12*) is predicted to have the largest transition dipole moment (0.48 D) (*8*). The ν_3 mode of C_5 is an "antisymmetric stretching mode" similar to ν_3 (σ_u^+) of C_3 near 2040 cm^{-1} (*3*). The ν_3 mode of C_3 is also predicted to have a remarkably strong transition dipole moment of 0.44 D (*14*).

Our search for the high-resolution vibration-rotation spectrum of C_5 was successful. Guided by our preliminary results, C_5 has been detected in the laboratory by two reseach groups. Our astronomical measurements are in excellent agreement (*15, 16*) with the subsequent laboratory measurements.

On 17 January 1989, spectra of the prototypical obscured carbon star IRC+10216 and the moon were observed with an unapodized resolution of 0.010 cm^{-1} (1.4 km s^{-1}, full width at half-maximum) by means of the Kitt Peak National Observatory 4-meter telescope and the Fourier transform spectrometer located at the coudé focus (*17*). The 218-min integration on IRC+10216 resulted in a peak signal-to-noise (1 SD) ratio of 360. The spectrum was limited to 2115 to 2195 cm^{-1} by a cold blocking filter. The moon, which is an intrinsically featureless source in the 2100 to 2200 cm^{-1} region, was observed at the same air mass as IRC+10216. We used the ratio of the lunar spectrum, which had a peak signal-to-noise ratio of 460, to the IRC+10216 spectrum to remove the telluric spectrum.

The observed 2170-cm^{-1} line positions of C_5 needed to be corrected for the Doppler shift caused by the motion of the circumstellar shell relative to the Fourier transform spectrometer. To do this we assumed, in analogy to other molecules observed in the infrared with similar line shape and excitation temperature (see below), that the lines exist in the circumstellar shell at the terminal expansion velocity, −14 km s^{-1}, relative to the center of mass (*18*). We used this velocity and corrected for a local standard-of-rest velocity of −26 km s^{-1} for IRC+10216 (*19*) and for the earth's velocity at the time of observation to measure the frequencies. Telluric ozone lines (*20*) were used to obtain the frequency zero point.

In the spectrum (Fig. 1), a series of six

Table 1. Line positions of C_5 observed in the 4.6-μm spectrum of IRC+10216.

Line	Frequency (cm^{-1})	Central depth* (%)
P(28)†	2164.347	1.9
P(26)	2164.733	2.1
P(20)	2165.870	2.3
P(18)	2166.241	2.3
P(16)	2166.612	2.4
P(14)	2166.977	2.9
P(12)	2167.339	3.9
P(10)	2167.699	2.4
P(8)	2168.052	3.1
R(6)	2170.613	2.8
R(14)	2171.901	3.5
R(16)	2172.214	3.6
R(18)†	2172.525	3.6
R(22)†	2173.135	3.7
R(24)	2173.433	3.2
R(26)	2173.731	2.8

*The C_5 lines are underresolved, so the linewidths (full width at half-maximum) of 0.010 cm^{-1} are determined by the instrumental resolution. †Slightly blended lines with higher uncertainties.

P. F. Bernath, Department of Chemistry, University of Arizona, Tucscon, AZ 85721.
K. H. Hinkle, Kitt Peak National Observatory, National Optical Astronomy Observatories, Tucson, AZ 85726.
J. J. Keady, Theoretical Division, Los Alamos National Laboratory, Los Alamos, NM 87545.